Electrochimica Acta 453 (2023) 142359

Contents lists available at ScienceDirect

Electrochimica Acta

journal homepage: www.journals.elsevier.com/electrochimica-acta

Revealing mechanisms of activated carbon capacity fade in lithium-ion capacitors

Obinna Egwu Eleri [a,b], Frederik Huld [a,b], Julie Pires [a], Wakshum Mekonnen Tucho [c], Philipp Schweigart [d], Ann Mari Svensson [d], Fengliu Lou [a,*], Zhixin Yu [b,*]

[a] Beyonder AS, 4313 Sandnes, Norway
[b] Department of Energy and Petroleum Engineering, University of Stavanger, 4036 Stavanger, Norway
[c] Department of Machine, Building and Materials Technology Laboratory IMBM, University of Stavanger, 4036 Stavanger, Norway
[d] Department of Materials Science and Engineering, Norwegian University of Science and Technology, 7491 Trondheim, Norway

ARTICLE INFO

Keywords:
Activated carbon
Electrolyte decomposition
Capacity fade
Lithium-ion capacitors

ABSTRACT

The capacity fade mechanism of activated carbon (AC) electrode in Li-ion electrolyte was studied via electrochemical impedance spectroscopy (EIS) and post-mortem electrode characterizations at different stages of electrochemical cycling. Electrochemical cycling was conducted in half cells incorporating the AC working electrode, Li metal counter electrode, and 1 M $LiPF_6$ in EC:DMC (1:1) electrolyte. Three phases were identified during the ageing process that corresponded with transformation of the passivation layer at the electrode surface and charge transfer impedance derived from the EIS analysis. Surface area and morphology analysis showed that the AC surface was progressively transformed by degradation products that reduced the available surface area and accessibility of electrolyte moieties into the pores. X-ray photoelectron spectroscopy suggested that the degradation products are from the $LiPF_6$ salt decomposition and carbonate solvent decomposition, while Raman analysis demonstrated increased defects in the electrode as cycling progressed. The capacity fade was therefore caused by the synergistic effect of electrolyte degradation and active material transformation.

1. Introduction

Global climate awareness on the adverse impact of fossil fuel powered energy sources has prompted the electrification of previously fossil dominated technologies such as automobiles and stationary power systems. Lithium-ion capacitors (LiC) are excellent in satisfying such operations due to the synergistic effect of combining conventionally high power capacitor cathode such as activated carbon (AC) and energy rich battery-type intercalation anode such as graphite in the LiC device architecture [1,2]. Consequently, charge storage in LiC occur via ion adsorption/desorption on the cathode and lithium intercalation/de-intercalation on the anode. As such, the LiC possesses higher power densities than lithium-ion batteries(LiB) but lower energy densities [2]. The lower energy densities are attributed to the low capacity of the AC cathode (<60 mAh/g) by virtue of its predominantly physical surface charge storage process, which limits the attainable specific energy especially when compared to intercalation type cathodes (e.g., lithium iron phosphate) used in LiB [3]. Many researchers have attempted to improve the energy density of the LiC while maintaining the high-power requirements by expanding the operating potential window of the AC cathode [4–6].

Typically, electrolytes consisting of lithium salts such as $LiPF_6$ dissolved in carbonate solvents such as ethylene carbonate (EC), dimethyl carbonate (DMC), ethyl methyl carbonate (EMC) and diethyl carbonate (DEC) are incorporated in LiC to realize wide operating potential window, good conductivity, and anode and Al current collector passivating abilities of EC and $LiPF_6$ salt [7,8]. However, the high specific surface area and often unavoidable presence of surface oxygenated species on the AC electrode can negatively affect the realisable operating potential window and device cycle life due to parasitic reactions with electrolyte constituents [9,10]. The EC solvent may continuously decompose and form a passivating solid porous layer on the surface [11,12]. Furthermore, the highly sensitive PF_6^- anion is prone to hydrolysis and oxidation as it contacts the polarized AC cathode [13,14]. These could consequently lead to the formation of by-products such as PF_5 and HF that may catalyse other cellular component degradation and cause interfacial instabilities [13,15,16].

The electrolyte degradation process proceeds via PF_6^- and EC

* Corresponding authors.
E-mail addresses: fengliu@beyonder.no (F. Lou), zhixin.yu@uis.no (Z. Yu).

https://doi.org/10.1016/j.electacta.2023.142359
Received 27 January 2023; Received in revised form 31 March 2023; Accepted 3 April 2023
Available online 4 April 2023
0013-4686/© 2023 The Author(s). Published by Elsevier Ltd. This is an open access article under the CC BY license (http://creativecommons.org/licenses/by/4.0/).

oxidation by F-abstraction and H-abstraction, subsequent to the parasitic faradaic reactions with oxygenated functionalities and moisture trapped in the AC pores [13,17]. Eventually, the cycle life of the device is affected as the electrolyte solvents and ionic moieties become depleted, and the surface of the AC cathode is passivated by the precipitated degradation products. Other contributors to capacity fade include binder decomposition, active material pulverization and gas generation, which can increase resistance and accelerate cycle life deterioration [18]. Mitigating such processes require in-depth investigation into how they occur and correlation of physical changes on the electrode surface with electrochemical state of the cell. Post-mortem analysis and in-situ/ex-situ spectroscopic techniques are therefore vital towards unravelling the causes of capacity fade and device failure.

Most of the previous studies have been conducted on the AC electrodes in supercapacitors utilizing $TEABF_4$ salt dissolved in propylene carbonate or acetonitrile solvent [18–20]. However, the use of Li-ion salts ($LiPF_6$) with the reactive PF_5, and the passivation film forming abilities of carbonate-based solvents (EC) have necessitated that the capacity fade mechanisms need to be revisited. Moreover, although the capacity fade mechanisms are related to the loss of active surface area and AC electrode modification by degradation products, the products remain largely unknown. Revealing the capacity fade mechanisms can thus provide measures via which they can be mitigated. In this regard, the nature, quantity, and when the degradation products are formed are to be studied. In addition, detrimental physio-chemical changes on the electrodes can be controlled via the incorporation of additives to either solubilize the degradation products or delay their formation.

In this study, the AC was characterized at different stages spanning before and after electrochemical cycling, using nitrogen physisorption, x-ray photoelectron spectroscopy (XPS), scanning electron microscopy (SEM) and Raman spectroscopy. The capacity retention was investigated via sequential floating voltage holds at 4.2 V, with electrochemical impedance spectroscopy (EIS) measurement acquired intermittently. The capacity fade was correlated with the EIS spectra and results from the AC characterization.

2. Experimental

2.1. Materials

Commercial activated carbon (YEC-8B) was purchased from Fuzhou Yihuan Carbon Co., Ltd. Lithium hexafluorophosphate ($LiPF_6$) (purity 99.94%), lithium chips, EC and DMC (purity 99.9%), polytetrafluoroethylene (PTFE) (60 wt.%) were purchased from Sigma Aldrich. The electrolyte 1 M $LiPF_6$ in EC:DMC (1:1) vol/vol was prepared by mixing the components in an Argon glove box with moisture and oxygen levels less than 0.1 ppm.

2.2. Electrode fabrication

Self-standing electrodes were assembled by mixing 92 wt.% AC powder and 8 wt.% PTFE binder into a dough, and roll pressed at 80 °C. The self-standing electrode was thereafter laminated at 160 °C onto a double-sided carbon coated Al current collector, with the aid of a hot rolling press (MTI-Corp). 15 mm discs were punched from the laminated electrode, weighed, and dried overnight in a vacuum oven at 140 °C. The active material thickness and loading was 100 μm and 6.7 mg/cm^2, respectively. After drying, the discs were transferred to the Argon glove box for cell assembly.

2.3. Cell assembly and electrochemical cycling

Half cells incorporating AC as the working electrode and lithium metal as the counter/reference electrode in CR2032 type coin cells were assembled in the glove box. Cellulose TF4030 (19 mm Ø) was used as the separator and 100 μl of the prepared electrolyte was added in each cell. The assembled cells were subjected to galvanostatic charge and discharge (GCD) cycling at different current densities (0.1C for 3 cycles, 0.5 C for 3 cycles, 1C, 2C, 5C, 10C, 20 C, 1C and 10C for 5 cycles; 1C = 42.6 mAh/g) in the potential range 3.0–4.2 V. The floating voltage ageing protocol consisted of a floating voltage hold (FVH) at 4.2 V for 10 h with consecutive capacity checks at 10C before and after each floating sequence to monitor the capacity fade. EIS was acquired after every cumulative 100 h of floating on the cycled cells. The EIS measurements were conducted in the frequency range 100 kHz to 0.01 Hz with an amplitude of 5 mV. The EIS spectra were fitted using the impedance.py package in PYTHON.

2.4. Sample characterization

Cell disassembly was carried out in the Argon glovebox. The cells were de-crimped using a custom type CR2032 de-crimper (Hohsen). The extracted AC electrodes were washed in a DMC solution to rinse off excess electrolyte and dried for 24 h under vacuum in the anti-chamber of the glove box.

Nitrogen physisorption analysis was performed using a Tristar II micromeritics surface and pore volume analyser. The specific surface area and pore volumes were determined using the Brunauer-Emmett-Teller (BET) and Nonlocal Density functional theory (NLDFT) methods. Samples were degassed for 24 h at 80 °C prior to measurements, while ensuring limited exposure to ambient atmosphere during handling. Surface morphology examination was conducted using Supra 35VP (ZEISS) field emission gun scanning electron microscope (FEG-SEM). Raman spectra were obtained using a Renishaw InVia Qontor Raman Microscope. The spectra were acquired using a 532 nm laser wavelength, x20 objective lens, exposure time of 20 s and 3 accumulations. XPS data were collected with a Thermo Scientific ESCALAB 250 spectrometer, using a focused monochromatized Al Kα radiation ($h\nu$ = 1486.6 eV). The pressure was maintained at 10^{-8} mbar and charge neutralization was applied. The analysed area of the samples was an ellipse with a dimension of 450 × 900 μm. The XPS introduction chamber was directly connected to an argon glovebox to protect the sample from any contact with air and moisture during the transfer. Spectra deconvolution and peak fitting was performed using Origin software and Gaussian peak fits.

3. Results and discussion

3.1. Electrochemical analysis

The capacity retention during the floating voltage is presented in Fig. 1, while the rate performance and respective charge/discharge curves at different C-rates are displayed in Figure S1 in Supporting Information (SI). The AC electrode endured up to 950 h of floating voltage

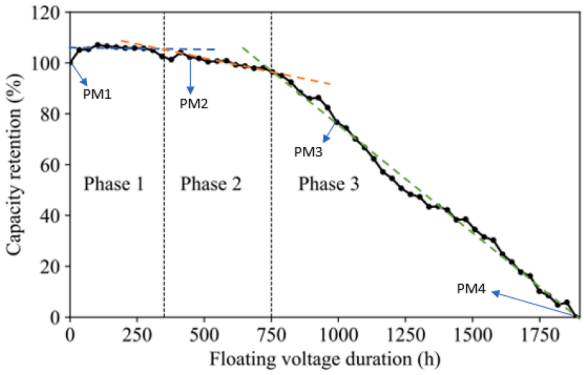

Fig. 1. Capacity retention during the floating voltage stability test; three distinct phases of capacity fade were identified. The arrows mark the FVH time points when the samples were obtained.

prior to reaching 80% capacity retention and approximately 1900 h before reaching 0% capacity retention. The ageing profile could be divided into three phases (denoted by the dashed lines) based on the distinct features and slope of the capacity retention profile. The exact position of the phases was determined by fitting the data to straight lines with varying slopes and marking the intersection of the lines. The phases corresponded to the capacity retention profile with three distinct features. Phase one is characterised by an initial increase in capacity, followed by a stable period which can be fitted to a horizontal straight line. After 350 h, the capacity retention decreases very slowly up to 750 h. The third phase is characterized by accelerated capacity fade in a steep slope until 0% capacity retention at 1900 h.

Samples for the post-mortem (PM) analysis were obtained at the respective positions denoted by PM in Fig. 1, to reveal the changes of the AC electrode surface. These points coincided with the state of the AC at different phases and was correlated with the capacity fade. The AC electrode after 450 h of FVH was without any visible capacity fade but was also studied to disclose possible surface transformations in phase two. The results from the post-mortem characterizations are presented in Section 3.2. All the characterized samples are summarized in Table 1.

The floating voltage stability test was complemented by EIS to reveal changes at the active material/electrolyte interfaces in relation to the state of capacity retention of the cell. The EIS spectra were acquired before floating (0 h) and after every 100 h of floating until 950 h when the cell was at 80% capacity retention, and periodically until 1900 h when the cell was at 0% capacity retention. The obtained EIS spectra are presented in Fig. 2a. The spectra were characterized by two semi circles at the high to medium frequency regions associated with the passivation layer impedance (Rp) and charge transfer impedance (Rct), a 45-degree sloping line at low frequencies attributed to Warburg diffusion (W) impedance, and a vertical straight line representing the capacitance (C). As the floating progressed, the spectra were gradually transformed at the high frequency region with the appearance of a conspicuous negatively sloped inverted line. The length and slope of this feature increased as the duration of ageing progressed. The origin of this feature was ambiguous and could be due to a capacitive behaviour/artefact which might have originated from the increasing active material and contact resistance usually obtained at high frequencies. To simplify the discussion, Rs was assigned to represent the bulk electrolyte resistance and active material/current collector contact resistance, which was the point at high frequency when the inverted sloping line intercepted with the real axis. The impedance spectra were fitted with similar circuits as reported in literature [21,22]. The evolution of the resistance Rs, Rp and Rct obtained from the fitting as the floating time progressed are presented in Fig. 2b. The deconvoluted R-CPE loops are illustrated in Figure S2 in SI, while the values of the fitting parameters are summarized in Table S1.

In Fig. 2b, Rs remained relatively constant in phase one as the floating voltage progressed, which implied that the bulk solution resistance and contact resistances were not altered in this phase and hence did not affect the capacity. On the contrary, Rp and Rct were 22 Ohm and 17 ohms before the floating but decreased significantly to around 5 ohms at the end of phase one. The trend for Rp and Rct in phase one suggests a reformation of the passivating deposits at the electrode interfaces owing to electrochemical activation and improved accessibility of electrolyte ions at the surface [22]. The electrochemical activation may have opened more pores on the AC surface for adsorption of the PF_6^- anions during the floating voltage charge, which resulted in the slight capacity increase. In phase two, the increase in Rs signalled electrolyte decomposition and accumulation of degradation products that coincided with a steady decrease in capacity. Meanwhile, the relatively stable Rp and Rct suggested that the initially formed passivating deposits remained unchanged. However, the overlayed R-CPE loops in Figure S2b and e, indicated some slight increase in Rp and Rct, which implied some transformation of the passivating deposits and increased charge transfer resistance. The capacity fade in phase two could have therefore been instigated by reduced accessibility of electrolyte moieties into the electrode surface, together with the effect of diminished PF_6^- anions for charge storage following the electrolyte decomposition.

In phase three, the capacity retention progressively decreased with a 45-degree slope line to near zero. On the contrary, the Rs value began to rise in a 45-degree trend, which inferred that electrolyte resistance/electrolyte degradation and accumulation of degradation products was substantially accelerated in this phase. Also, Rp and Rct increased significantly to 16 ohm and 12 ohm after 1400 h of floating, which was almost 3 times the value at the end of phase one. In contrast, the Rs increased to 47.8 Ohm after 1400 h, which was almost 10 times greater than the value at the end of phase one. This further implied that the electrolyte could have been substantially decomposed after 750 h, while the growth of the inverted vertical sloping peak at high frequencies (Fig. 2a) suggested that the artefact was strongly related to the electrochemical ageing of the cell since it considerably increased towards the end of life.

The initial deterioration up to 80% capacity retention (950 h) could have been dominated by transformation of the AC electrode surface by the degradation products and gradual reduction of PF_6^- anions. Nevertheless, the contribution of the lithium counter electrode cannot be ignored, because the rapidly expanded Rp in phase three could be attributed to the deposition of irregular aggregates of dead lithium and pulverization of the initial formed surface passivating film on the lithium counter electrode [23]. More active sites might have been created upon which electrolyte degradation was accelerated as indicated by the exponential increase in Rs. Hence, electrolyte starvation in phase three may have significantly contributed to the capacity fade in this phase.

Table 1
Denotations and descriptions of the samples.

Denotations	Descriptions
AC powder	Dried AC powder
AC electrode	Dried AC electrode
Blank electrode	AC electrode immersed in electrolyte (uncycled)
0 h of FVH	AC electrode after GCD cycles but 0 h of FVH (cell at 100% capacity retention)
450 h of FVH	AC electrode after 450 h of FVH (cell at near 100% capacity retention)
950 h of FVH	AC electrode after 950 h of FVH (cell at 80% capacity retention)
1900 h of FVH	AC electrode after 1900 h of FVH (cell at 0% capacity retention)

3.2. Degradation mechanism

The results from the electrochemical analysis using combined floating voltage and intermittent EIS analysis suggested transformations of the electrode surfaces as the capacity fade progressed. In this section, different characterization techniques are employed to reveal the nature of the surface changes and deposits on the electrodes at different stages, which contributed to the capacity fade.

SEM was used to probe the changes in surface morphology of the AC. From Fig. 3a and b, one can distinguish the effect of the PTFE binder as reflected by the fused and compacted nature of dry electrode, in contrast with the isolated grains of the AC powder. The compacted nature indicated a reduced surface area of the AC electrode when compared to the AC powder due to the PTFE binder penetration in the pores. Moreover, some aggregates of passivating deposited species were observed in the SEM image of the blank electrode (Fig. 3c). Therefore, by immersing the AC electrode in the electrolyte, though without cycling, the passivating deposits may have covered some of the available surface area or occupied the pores. The passivating deposits are likely formed from reactions between the electrolyte species and oxygen functionalities on the surface of the AC electrode [11,12,24].

The electrode at 0 h of FVH had undergone few GCD cycles but exhibited similar passivating deposits at the surface (Fig. 3d). However,

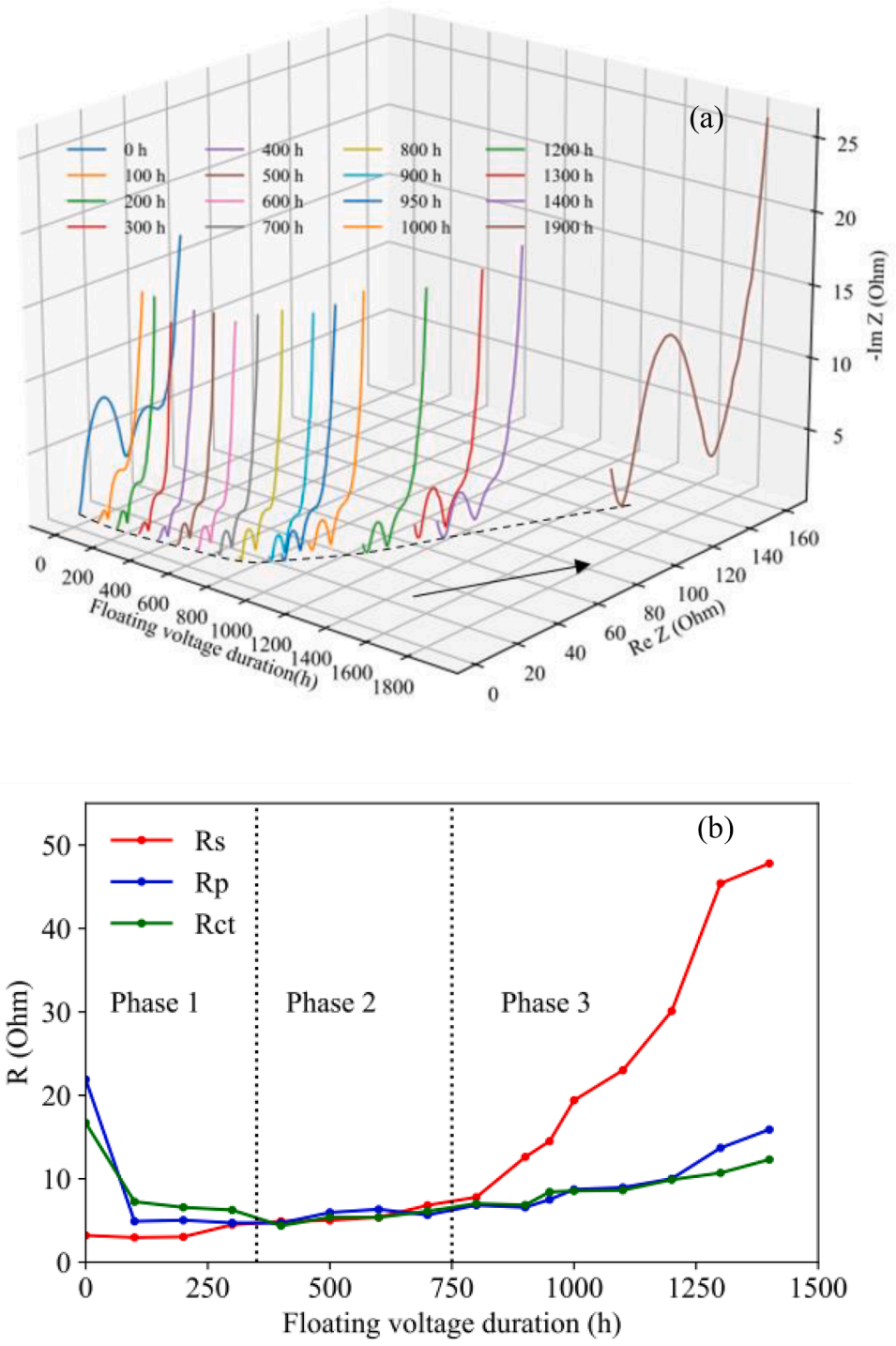

Fig. 2. (a) 3D EIS spectra after different durations of floating; (b) Resistance parameters (Rs, Rp, Rct) after fitting.

the edges of the AC grains appeared to be etched, possibly from electrochemical activation due to the cycling [25]. As cycling progressed towards phase two (450 h of FVH) and three (950 h of FVH), the passivating deposits increased due to substantial deposition of insoluble electrolyte degradation products (Fig. 3e and f). Therefore, the capacity fade could be related to the loss of surface area and pores for ion adsorption.

At 1900 h of FVH (Fig. 3g) with 0% capacity retention, the AC electrode surface was completely covered by the aggregated decomposition products and appeared to be of a fused nature. In addition, some new spherical deposits were observed. EDX analysis of these spherical spots (Figure S3) revealed that they were predominantly composed of carbon (69%), oxygen (8%), fluorine (20%) and phosphorus (2%), which are elemental constituents of the electrolyte and electrolyte degradation products.

Nitrogen physisorption analysis was used in probing the pore property transformation at different stages. The physisorption isotherms (Fig. 4a) display type I/IV characteristic according to the IUPAC classification, with predominantly micropores and some mesopores in the AC powder. The incorporation of the PTFE binder reduced the surface area and pore volume by around 20% and 7% (Fig. 4b). The reductions occurred mostly in the micropores where some of the PTFE binder was

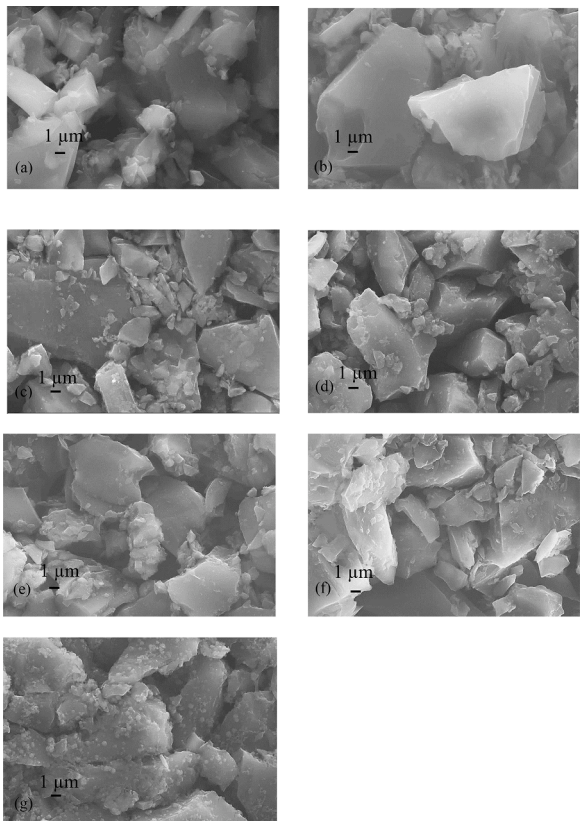

Fig. 3. SEM images of the (a) AC powder, (b) AC electrode, (c) Blank electrode, AC electrode at (d) 0 h of FVH, (e) 450 h of FVH, (f) 950 h of FVH, and (g) 1900 h of FVH. All images were taken at 10 000X magnification.

absorbed, while the slight reduction in the mesopores was due to compaction during the electrode fabrication process. The appearance of a hysteresis loop upon contact with the electrolyte (blank electrode) and further growth upon electrochemical cycling (0 h of FVH), inferred that the pore structure of the AC electrode was indeed modified by the electrochemical process.

Further reductions in surface area and pore volume were observed as the AC electrode (Blank electrode) was contacted with the electrolyte. The reductions are in accordance with the observed passivating deposits in SEM study. The AC electrode at 0 h of FVH had a remarkable increase in micropores compared to the blank electrode, although the total surface area and pore volume decreased. Therefore, the electrochemical activation process increased the micropores for charge storage and was responsible for the increased capacity retention beyond 100% in phase one [25–28]. The electrochemical activation may have opened pores that were blocked by the passivating deposits, although the decrease in total surface area and pore volume may be related to slight electrolyte degradation after the few GCD cycles. At 950 h of FVH, the surface area and pore volume decreased further, which inferred that electrolyte decomposition continued. The approximately 20% capacity loss was commensurate with the reduction in micropore volume after comparing the cumulative volume of micropores of the electrode (0.3491 cm^3/g) with the initial volume at 0 h of floating (0.4662 cm^3/g). This was expected, since the micropores were predominantly where ion adsorption and charge storage occurred. Moreover, the isotherm at 950 h of FVH was slightly modified, with a more pronounced hysteresis loop occurring within relative pressure of 0–0.4, in contrast with the barely visible hysteresis loop at 0 h of FVH. Hence, the pores were also modified by possible reactions with electrolyte degradation products such as HF and PF_5 that could erode active material and passivating deposits [13,29]. Furthermore, at 950 h of FVH, the electrode further broadened the pore size distribution, with the presence of larger micropores around 1.4–1.6 nm and smaller micropores < 0.8 nm.

It was interesting to observe that the AC electrode at 1900 h of FVH still retained around 40–50% of the original surface area and pore volume. Thus, the failure in phase three could be certainly ascribed to the loss of ionic species from accelerated electrolyte degradation caused by electrode structural integrity alteration and eventual pulverization.

We further employed XPS to study the surface species evolution at different stages. The C1s spectra of the AC powder revealed the presence of six peaks at binding energies of 283.7, 284.2, 284.9, 285.5, 286.8 and 288.9 eV, corresponding to sp (C≡C), AC (C = C), CH_x (C—C), C—OH, C—O and C = O surface groups (Fig. 5a). The C = C peak was characteristic of AC due to the abundant sp^2 like species and is correlated to the activation temperature [30]. The elemental composition of the AC powder was determined to be carbon (97.7%) and oxygen (2.3%). The C1s spectra of the AC electrode (Fig. 5b) revealed similar peaks as the AC powder but with a new peak at 291.9 eV, corresponding to the CF_2 group from the PTFE binder. The oxygenated functionalities on AC are responsible for electrolyte degradation and the passivating deposits observed at the surface of the blank electrode (Fig. 3c) [11,12,24].

The deconvoluted C1s, F1s and P2p spectra of electrodes after contact with the electrolyte are presented in Fig. 6. The C1s spectra of the blank electrode (Fig. 6a) showed peaks at 284.2, 286.5, 288.2, 290.1 and 291.9 eV, assigned to the C = C, C—O, C = O, CO_3 and CF_2 groups. The disappearance of the sp peak indicate that some carbon species were reacted. It is also interesting to see that the asymmetric conducting carbon shape was modified, and the PTFE intensity was increased in comparison to the C1s spectra of the AC electrode (Fig. 5b). The increased CF_2 intensity suggests that contact with the electrolyte exposed more PTFE at the surface after reacting with the oxygenated carbon species on the AC electrode. In the P2p spectra, $Li_xPO_yF_z$ and polyphosphates were identified at 133.7 and 235.5 eV, while LiF, $Li_xPO_yF_z$ and CF_2 species were identified at 685.1, 686.4 and 689.1 eV in the F1s spectra. These species together with the oxygenated carbon species are the products of $LiPF_6$ and the carbonate solvent decomposition after nucleophilic attack by surface oxygen species and moisture in the pores. Moreover, the LiF species could also come from the ion paired $LiPF_6$. LiF and PF_5 are the equilibrium decomposition products of ion paired $LiPF_6$, which is commonly present in incompletely dissociated $LiPF_6$ [13,17,31]. PF_5 is also responsible for inducing solvent degradation and other parasitic reactions that may form HF, which is detrimental to active material and interfacial stability [13,17,31].

The diminished AC peak in the C1s spectra for the electrode at 0 h of FVH (Fig. 6a) and the increase of the PTFE peak and oxygenated carbons are ascribed to surface passivation and continued electrolyte salt and carbonate solvent decomposition. Furthermore, the F1s and P2p spectra of the electrode at 0 h of FVH (Fig. 6b and c) showed increased intensities of LiF and phosphate species, confirming enhanced electrolyte degradation after the few GCD cycles. This correlates with the reduced surface area from the nitrogen physisorption analysis.

The C1s spectra of the electrodes after 450 h of FVH and at 950 h of FVH exhibited similar oxygenated carbon species. The further diminished AC peak signified intense surface coverage of the electrode, while the increased CF_2 band suggested exposed/exfoliated binder after surface restructuring. The P2p and F1s spectra showed increased presence of phosphates, $Li_xPO_yF_z$ and LiF, with the latter being the dominant specie. Thus, the capacity fade observed in phase three was caused by enhanced anion decomposition. This was in combination with restricted access of the already depleted ionic moieties to the pores of the AC electrode with decreased pore volumes.

At 1900 h of FVH, it was interesting to see that the intensity of AC was significantly increased, in comparison with the electrode after 950 h of FVH. We speculate that this may be related to the spherical amorphous specie observed in SEM (Fig. 3g) or caused by AC electrode pulverization from possible binder degradation. Moreover, the disappearance of the CF_2 band at 1900 h of FVH suggested that either

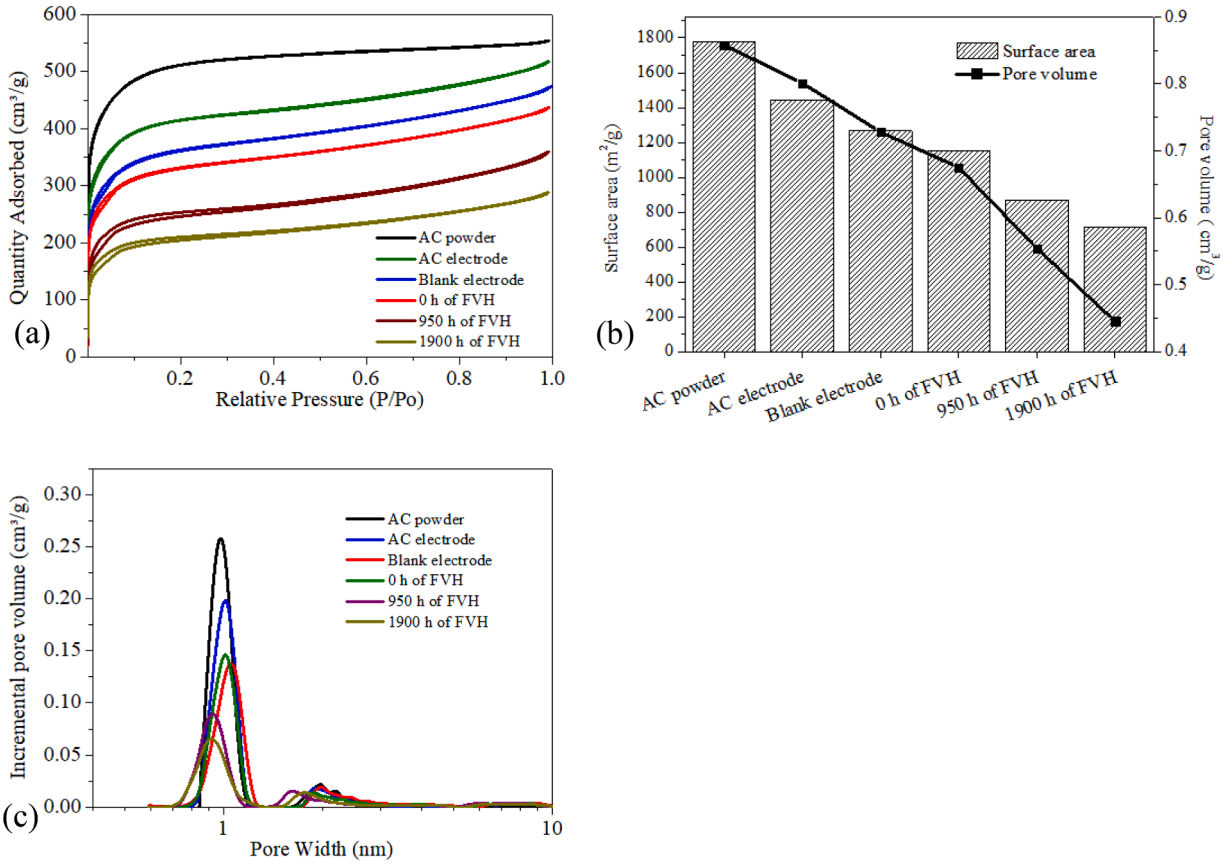

Fig. 4. (a) Nitrogen adsorption and desorption isotherms, (b) BET Surface area and pore volume, (c) Pore size distributions of AC powder and different AC electrodes.

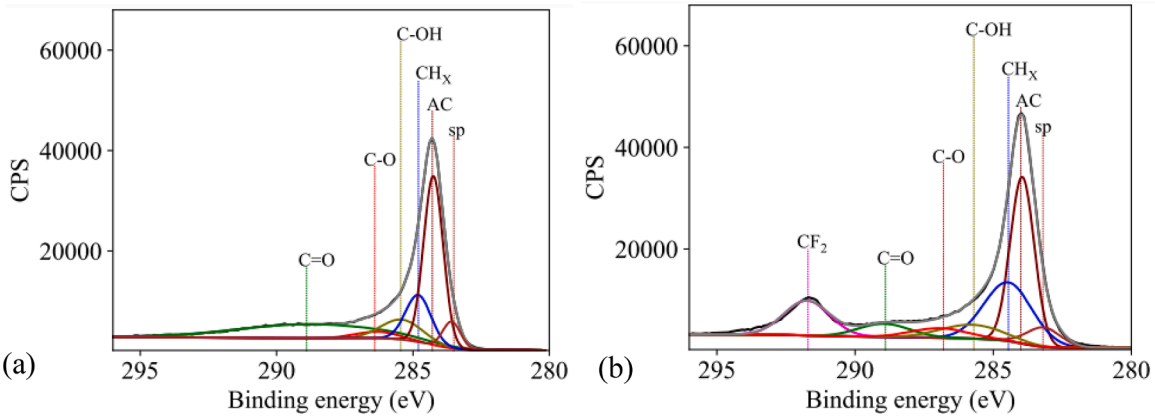

Fig. 5. Deconvoluted C1s spectra of (a)AC powder, (b) AC electrode.

the AC electrode surface was completely covered by this newly deposited amorphous carbon, or the PTFE binder reacted with adsorbed lithium on the surface of the electrode. Although PTFE is known to be very stable and unreactive, it could be reduced upon contact with lithium to form an amorphous carbon specie and LiF, as shown below [29]:

$$-(-CF_2-)_n - + 2n\,Li \rightarrow n\,C(amorphous) + 2n\,LiF$$

The presence of AlO_xF_y species in the F1s spectra at 1900 h of FVH (Fig. 6b) supports fluorinated attack of the current collector, which could indicate the pulverization of the AC electrode. Meanwhile, the increased $Li_xPO_yF_z$ and phosphates species signify total salt degradation at 1900 h of FVH (Fig. 6c).

Raman spectroscopy was conducted to investigate changes in graphitic order and defects during floating. The spectra were deconvoluted using origin software and exhibited five peaks as illustrated in Fig. 7a. The two prominent peaks at around 1350 and 1580 cm^{-1} are the characteristic D and G bands. The latter is attributed to the in-plane vibrations of sp^2 hybridized carbon, while the former is attributed to out of plane vibrations arising from structural defects and multiphases in the carbon structure [32]. The D_1 band at 1179 cm^{-1} is assigned to impurities in the graphitic lattice, while the D_2 band at 1493 cm^{-1} corresponds to the stacking defects in the graphene layer [32] and the presence of sp^2 amorphous carbon [33]. The D_3 band at 1653 cm^{-1} is assigned to disorder in the surface graphene layers [32,34,35].

The defect ratio was calculated from the intensities of the D and G band (Fig. 7b). The defect level increased as the AC powder was

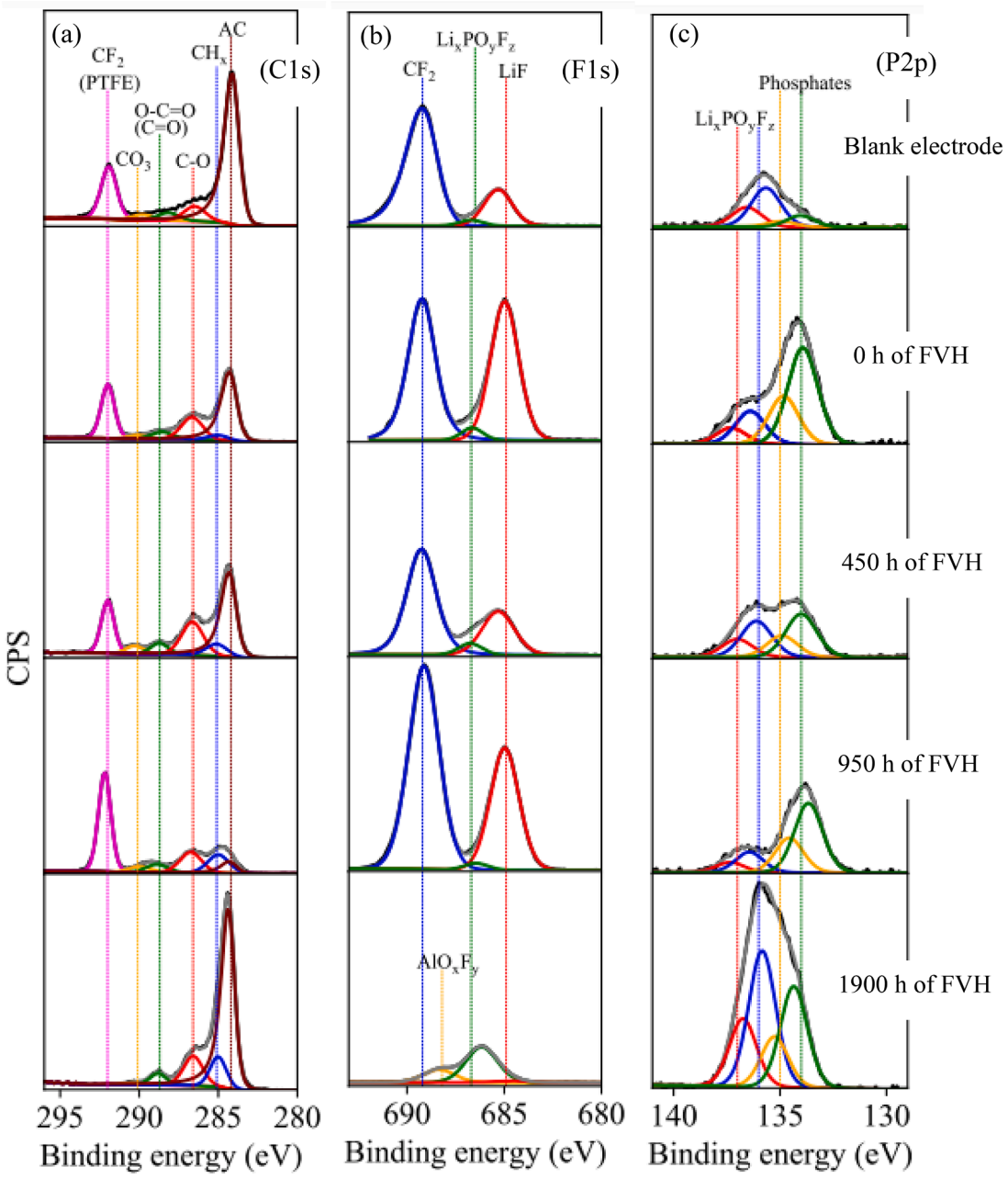

Fig. 6. Deconvoluted XPS spectra showing the (a) C1s, (b) P2p, and (c) F1s peaks of the AC electrode at different stages of FVH after contact with the electrolyte.

transformed to the AC electrode and subjected to electrochemical cycling. The defects originated from PTFE addition and deposits of electrolyte degradation products at the AC surface. Moreover, the decrease in the defect ratio after 450 h of FVH was caused by increased graphitization as evidenced by the band intensities (Fig. 7c). The band intensities in Fig. 7c showed that the D and G band increased in a continuous trend until the plateau at 450 h of FVH. Beyond this point, increased D_2 bands were responsible for the increased defects since the other defective bands (D_1 and D_3) remained relatively the same.

At 950 h of FVH, the defect ratio increased again and reached maximum after 1900 h of FVH. Hence, increased defects also contributed to the capacity fade. The increased defect level is synonymous with increased electrode resistance and reduced particle to particle conductivity [36]. Moreover, the continuously increasing D_2 band at 950 h and 1900 h of FVH meant that the stacking defects in the graphitized carbon structure was significant. Besides, it might also be related to the increased presence of sp^2 carbons formed after electrochemical oxidization of the AC electrode by electrolyte species or binder exfoliation and electrode pulverization discussed earlier.

4. Conclusion

The causes of capacity fade in LiC have been investigated via a combination of intermittent EIS during floating voltage ageing and post-mortem characterization of the AC electrode at different electrochemical states. Three phases were identified during the floating voltage that corresponded to different electrochemical processes occurring in the cell in relation to the capacity fade. The first phase was assigned to the modification of the formed passivating deposits on the electrodes that permitted increased access of electrolyte species into the pores and the observed rise in capacity. The second phase marked the effect of electrolyte decomposition with gradual decrease in capacity, which was caused by PF_6 anion and other electrolyte species degradation. Here, the passivating deposits was built up progressively by the deposition of

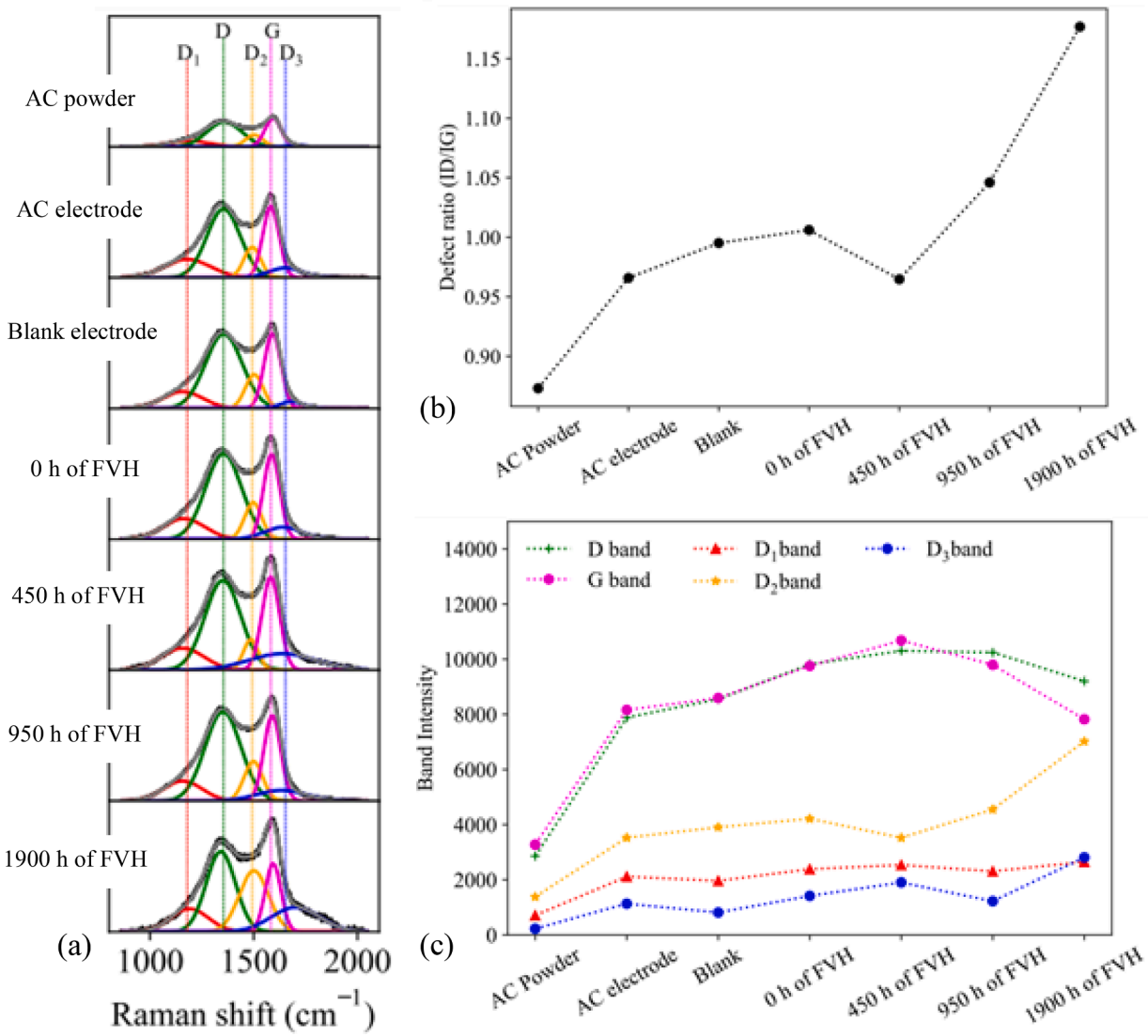

Fig. 7. (a) Deconvoluted Raman spectra, (b) Defect ratio, and (c) Comparison of band intensities of the activated carbon electrode at different stages. The I_d/I_g ratio was calculated from the intensity of the D and G bands.

degradation products. XPS study showed that the products consist of oxygenated carbon species, lithium fluorophosphates, lithium fluoride and polyphosphate species. Their presence resulted in the gradual reduction of available surface area of the AC electrode. In the third phase, electrolyte degradation was accelerated with a steep 45-degree slope in capacity reduction. We suppose that a combination of increased degradation products such as HF and PF_5 were responsible for catalysing solvent degradation and eventual depletion of the electrolyte moieties. Furthermore, the electrode at 80% capacity retention had increased phosphates and lithium fluoride as well as diminished AC peak, which suggested severe surface coverage by insoluble degradation products. Other factors such as increased defect ratio and growth of defective bands consisting of sp^2 hybridized species were possible contributors to the capacity fade via reduced conductivity.

We propose that strategies towards extending the cyclic stability and delaying the electrolyte degradation on AC cathodes should be targeted at improving the anion oxidation resistance. That would reduce the deposition of polyphosphates and other anion/$LiPF_6$ salt degradation products on the surface of the AC. Further measures could be the incorporation of additives to improve $LiPF_6$ dissociation and reduce ion pairing, additives for PF_5 and HF scavenging, incorporation of alternative anions with superior electrochemical stabilities, and solvent optimization to improve anion stability. These approaches could extend the phase one region in the capacity retention profile after engineering the passivation layer to be sufficiently resistive towards attack by degradations products. The added benefit of delaying the transition towards phase two where anion degradation commences in full could also be attained.

CRediT authorship contribution statement

Obinna Egwu Eleri: Conceptualization, Data curation, Formal analysis, Investigation, Visualization, Methodology, Writing – original draft, Writing – review & editing. **Frederik Huld:** Formal analysis, Investigation, Methodology, Writing – review & editing. **Julie Pires:** Formal analysis, Investigation, Methodology, Validation, Writing – review & editing. **Wakshum Mekonnen Tucho:** Investigation, Formal analysis, Resources, Methodology. **Philipp Schweigart:** Investigation, Validation, Writing – review & editing. **Ann Mari Svensson:** Resources, Validation, Writing – review & editing. **Fengliu Lou:** Conceptualization, Funding acquisition, Methodology, Validation, Resources, Project administration, Supervision, Writing – review & editing. **Zhixin Yu:** Validation, Funding acquisition, Resources, Project administration, Supervision, Writing – review & editing.

Declaration of Competing Interest

The authors declare that they have no known competing financial interests or personal relationships that could have appeared to influence the work reported in this paper.

Data availability

Data will be made available on request.

Acknowledgements

The authors gratefully acknowledge the Research council of Norway and Beyonder AS for financial support of the project under the Industrial PhD project scheme grant number 311678. The authors would also like to thank Professor Remi Dedryvere (University of Pau) for assistance with the XPS analysis.

Supplementary materials

Supplementary material associated with this article can be found, in the online version, at doi:10.1016/j.electacta.2023.142359.

References

[1] G.G. Amatucci, F. Badway, A. Du Pasquier, T. Zheng, An asymmetric hybrid nonaqueous energy storage cell, J. Electrochem. Soc. 148 (8) (2001) A930.
[2] K. Naoi, S. Ishimoto, J.-i. Miyamoto, W. Naoi, Second generation 'nanohybrid supercapacitor': evolution of capacitive energy storage devices, Energy Environ. Sci. 5 (11) (2012) 9363–9373.
[3] S.R. Sivakkumar, A. Pandolfo, Evaluation of lithium-ion capacitors assembled with pre-lithiated graphite anode and activated carbon cathode, Electrochim. Acta 65 (2012) 280–287.
[4] S. Dsoke, Expanding the Cathodic Potential Window of Activated Carbon Electrodes in a Lithium-Salt Containing Electrolyte, Batteries Supercaps. 1 (6) (2018) 215–222.
[5] O.E. Eleri, K.U. Azuatalam, M.W. Minde, A.M. Trindade, N. Muthuswamy, F. Lou, Z. Yu, Towards high-energy-density supercapacitors via less-defects activated carbon from sawdust, Electrochim. Acta 362 (2020), 137152.
[6] H.-f. Xia, B. Zhang, C.-h. Wang, L. Cao, B. Luo, X.-m. Fan, J.-f. Zhang, X. Ou, Surface engineered carbon-cloth with broadening voltage window for boosted energy density aqueous supercapacitors, Carbon N Y 162 (2020) 136–146.
[7] L. Xing, X. Zheng, M. Schroeder, J. Alvarado, A. von Wald Cresce, K. Xu, Q. Li, W. Li, Deciphering the ethylene carbonate–propylene carbonate mystery in Li-ion batteries, Acc. Chem. Res. 51 (2) (2018) 282–289.
[8] S.-.T. Myung, Y. Sasaki, S. Sakurada, Y.-.K. Sun, H. Yashiro, Electrochemical behavior of current collectors for lithium batteries in non-aqueous alkyl carbonate solution and surface analysis by ToF-SIMS, Electrochim. Acta 55 (1) (2009) 288–297.
[9] M. Tokita, N. Yoshimoto, K. Fujii, M. Morita, Degradation characteristics of electric double-layer capacitors consisting of high surface area carbon electrodes with organic electrolyte solutions, Electrochim. Acta 209 (2016) 210–218.
[10] Z. Ding, V. Trouillet, S. Dsoke, Are functional groups beneficial or harmful on the electrochemical performance of activated carbon electrodes? J. Electrochem. Soc. 166 (6) (2019) A1004.
[11] F. Béguin, V. Presser, A. Balducci, E. Frackowiak, Carbons and electrolytes for advanced supercapacitors, Adv. Mater. 26 (14) (2014) 2219–2251.
[12] D. Stępień, Z. Zhao, S. Dsoke, Shift to post-li-ion capacitors: electrochemical behavior of activated carbon electrodes in li-, na-and k-salt containing organic electrolytes, J. Electrochem. Soc. 165 (11) (2018) A2807.
[13] J.G. Han, K. Kim, Y. Lee, N.S. Choi, Scavenging materials to stabilize LiPF6-containing carbonate-based electrolytes for Li-ion batteries, Adv. Mater. 31 (20) (2019), 1804822.
[14] C.L. Campion, W. Li, B.L. Lucht, Thermal decomposition of LiPF6-based electrolytes for lithium-ion batteries, J. Electrochem. Soc. 152 (12) (2005) A2327.
[15] H. Yang, G.V. Zhuang, P.N. Ross Jr, Thermal stability of LiPF6 salt and Li-ion battery electrolytes containing LiPF6, J. Power Sources 161 (1) (2006) 573–579.
[16] M.M. Thackeray, S.-.H. Kang, C.S. Johnson, J.T. Vaughey, R. Benedek, S. Hackney, Li 2 MnO 3-stabilized LiMO 2 (M= Mn, Ni, Co) electrodes for lithium-ion batteries, J. Mater. Chem. 17 (30) (2007) 3112–3125.
[17] O. Borodin, W. Behl, T.R. Jow, Oxidative stability and initial decomposition reactions of carbonate, sulfone, and alkyl phosphate-based electrolytes, J. Phys. Chem. C 117 (17) (2013) 8661–8682.
[18] P. Azaïs, L. Duclaux, P. Florian, D. Massiot, M.-.A. Lillo-Rodenas, A. Linares-Solano, J.-.P. Peres, C. Jehoulet, F. Béguin, Causes of supercapacitors ageing in organic electrolyte, J. Power Sources 171 (2) (2007) 1046–1053.
[19] P. Ruch, D. Cericola, A. Foelske, R. Kötz, A. Wokaun, A comparison of the aging of electrochemical double layer capacitors with acetonitrile and propylene carbonate-based electrolytes at elevated voltages, Electrochim. Acta 55 (7) (2010) 2352–2357.
[20] Y. Liu, B. Soucaze-Guillous, P.-.L. Taberna, P. Simon, Understanding of carbon-based supercapacitors ageing mechanisms by electrochemical and analytical methods, J. Power Sources 366 (2017) 123–130.
[21] Z. Shi, J. Zhang, J. Wang, J. Shi, C. Wang, Effect of the capacity design of activated carbon cathode on the electrochemical performance of lithium-ion capacitors, Electrochim. Acta 153 (2015) 476–483.
[22] X. Sun, X. Zhang, W. Liu, K. Wang, C. Li, Z. Li, Y. Ma, Electrochemical performances and capacity fading behaviors of activated carbon/hard carbon lithium ion capacitor, Electrochim. Acta 235 (2017) 158–166.
[23] K. Guo, S. Qi, H. Wang, J. Huang, M. Wu, Y. Yang, X. Li, Y. Ren, J. Ma, High-Voltage Electrolyte Chemistry for Lithium Batteries, Small Science 2 (5) (2022), 2100107.
[24] C. Tran, J. Kafle, X.-.Q. Yang, D. Qu, Increased discharge capacity of a Li-air activated carbon cathode produced by preventing carbon surface passivation, Carbon N Y 49 (4) (2011) 1266–1271.
[25] T. Zhang, B. Fuchs, M. Secchiaroli, M. Wohlfahrt-Mehrens, S. Dsoke, Electrochemical behavior and stability of a commercial activated carbon in various organic electrolyte combinations containing Li-salts, Electrochim. Acta 218 (2016) 163–173.
[26] M.M. Hantel, T. Kaspar, R. Nesper, A. Wokaun, R. Kötz, Partially reduced graphite oxide for supercapacitor electrodes: effect of graphene layer spacing and huge specific capacitance, Electrochem. Commun. 13 (1) (2011) 90–92.
[27] S. Mitani, S.-.I. Lee, K. Saito, S.-.H. Yoon, Y. Korai, I. Mochida, Activation of coal tar derived needle coke with K2CO3 into an active carbon of low surface area and its performance as unique electrode of electric double-layer capacitor, Carbon 43 (14) (2005) 2960–2967.
[28] T. Aida, I. Murayama, K. Yamada, M. Morita, High-energy-density hybrid electrochemical capacitor using graphitizable carbon activated with KOH for positive electrode, J. Power Sources 166 (2) (2007) 462–470.
[29] J. Kim, J.G. Lee, H.-s. Kim, T.J. Lee, H. Park, J.H. Ryu, S.M. Oh, Thermal degradation of solid electrolyte interphase (SEI) layers by phosphorus pentafluoride (PF5) attack, J. Electrochem. Soc. 164 (12) (2017) A2418.
[30] A. Lazzarini, A. Piovano, R. Pellegrini, G. Leofanti, G. Agostini, S. Rudić, M. R. Chierotti, R. Gobetto, A. Battiato, G. Spoto, A comprehensive approach to investigate the structural and surface properties of activated carbons and related Pd-based catalysts, Catal Sci Technol 6 (13) (2016) 4910–4922.
[31] D.M. Seo, O. Borodin, S.-.D. Han, Q. Ly, P.D. Boyle, W.A. Henderson, Electrolyte solvation and ionic association, J. Electrochem. Soc. 159 (5) (2012) A553.
[32] W. Chen, X. Zhou, S. Shi, N. Thiphuong, M. Chen, Synergistical enhancement of the electrochemical properties of lignin-based activated carbon using NH 3· H 2 O dielectric barrier discharge plasma, RSC Adv. 7 (12) (2017) 7392–7400.
[33] T. Jawhari, A. Roid, J. Casado, Raman spectroscopic characterization of some commercially available carbon black materials, Carbon N Y 33 (11) (1995) 1561–1565.
[34] A. Sadezky, H. Muckenhuber, H. Grothe, R. Niessner, U. Pöschl, Raman microspectroscopy of soot and related carbonaceous materials: spectral analysis and structural information, Carbon 43 (8) (2005) 1731–1742.
[35] M.A.d. Amaral, J.T. Matsushima, M.C. Rezende, E.S. Gonçalves, J.S. Marcuzzo, M. R. Baldan, Production and characterization of activated carbon fiber from textile PAN fiber, J. Aerospace Technol. Manag. 9 (2017) 423–430.
[36] P.T. Araujo, M. Terrones, M.S. Dresselhaus, Defects and impurities in graphene-like materials, Mater. Today 15 (3) (2012) 98–109.